Benchmark thermodynamic analysis of methylammonium lead iodide decomposition from first principles

Douglas Heine,[†] Hui-Chia Yu,[‡,¶] and Volker Blum[*,§]

[†]*Department of Mechanical Engineering, Michigan State University, East Lansing, MI*

[‡]*Department of Computational Mathematics, Science and Engineering, Michigan State University, East Lansing, MI*

[¶]*Department of Chemical Engineering and Materials Science, Michigan State University, East Lansing, MI*

[§]*Thomas Lord Department of Mechanical Engineering and Materials Science, Duke University, Durham, NC*

E-mail: volker.blum@duke.edu

Abstract

Hybrid organic-inorganic perovskites (HOIPs) such as methylammonium lead iodide ($MAPbI_3$) are promising candidates for use in photovoltaic cells and other semiconductor applications, but their limited chemical stability poses obstacles to their widespread use. *Ab initio* modelling of finite-temperature and pressure thermodynamic equilibria of HOIPs with their decomposition products can reveal stability limits and help develop mitigation strategies. We here use a previously published experimental temperature-pressure equilibrium to benchmark and demonstrate the applicability of the harmonic and quasiharmonic approximations, combined with a simple entropy correction for the configurational freedom of methylammonium cations in solid $MAPbI_3$

and for several density functional approximations, to the thermodynamics of $MAPbI_3$ decomposition. We find that these approximations, together with the dispersion-corrected hybrid density functional HSE06, yield remarkably good agreement with the experimentally assessed equilibrium between T=326 K and T=407 K, providing a solid foundation for future broad thermodynamic assessments of HOIP stability.

Introduction

Methylammonium (MA) lead iodide ($CH_3NH_3PbI_3$ or $MAPbI_3$) is a hybrid organic-inorganic perovskite (HOIP) semiconductor that has garnered much interest as a light-harvesting material for photovoltaic cells due to its facile synthesis and high power-conversion efficiency.[1–30] As a result of this development, certified power conversion efficiency of devices based on the HOIP paradigm has grown to more than 25.5% in recent years for single-junction cells,[31] reaching 26.1% in July 2023.[32] Tandem cells coupling HOIP and Si devices have rapidly increased in efficiency, reaching 33.7% certified efficiency in May 2023.[32] While exact composition data are not always immediately available for the latest devices, an earlier (2022) record device reached 31.3% efficiency in a device without $MAPbI_3$ and 30.9% in a device containing a small amount of $MAPbI_3$, respectively.[33] However, stability remains an ongoing research priority for hybrid metal halide based devices.[1–3,5–7,11–18,21,22,24,26,27,29,34,35] The prototypical compound $MAPbI_3$ tends to decompose when exposed to realistic operating conditions, most notably high temperatures and humidity.[1,2,7,10–18,22,24,27,29,34,35] Several approaches have been investigated to improve the lifespans of perovskite photovoltaic cells, such as encapsulating the cells with impermeable materials[1,3,5,6,24] and altering the chemical composition of the perovskites. For instance, methylammonium ions can be replaced with formamidinium ($CH_5N_2^+$)[36–38] or cesium.[11,38–40] Indeed, demonstrated device stability in methylammonium-free perovskite cells can reach 2,000 hours in the current literature,[6,7,16,21,24,26] but perovskite solar cell stability nevertheless remains an ongoing issue for technological viability over commercially relevant device lifetimes. Long-term stability remains a general research topic for

the much broader class of metal halide HOIPs.

One step towards developing mitigation strategies against decomposition is to assess thermodynamic stability boundaries of the broader class of HOIP materials in a given environment. Specifically, for assessing the effectiveness of encapsulation-based[1,3,5,6,24] strategies, it would be useful to be able to predict temperature-pressure equilibria of HOIPs with their decomposition products from first principles. However, $MAPbI_3$ and other hybrid perovskites present some difficulties with respect to computational modelling due to the strongly anharmonic nature of the organic-inorganic lattice. Specifically, the polarity and rotational asymmetry of the methylammonium ions introduce complex internal degrees of freedom to the material, causing the lattice around them to distort.[4,9,13,19,20,28,30,41–44] Depending on the temperature, these ions may be temporarily fixed by hydrogen bonds (at cryogenic temperatures[44]), they may switch between several minimum-energy orientations or they may even dynamically tumble.[41,44] Additionally, the orientational preferences of these ions causes the surrounding lattice to distort into non-cubic structures (specifically, orthorhombic and tetragonal phases) at low temperatures. One option is to apply ab-initio molecular dynamics and thermodynamic integration of anharmonic terms to the problem of $MAPbI_3$ thermodynamics and decomposition,[28,41,45] but this method is computationally demanding, with either significant computational cost (if carried out by a direct first-principles approach) or a nontrivial workflow by machine-learning (ML) an interpolated potential energy surface with lower computational cost and sufficient precision.[4,27] For simpler solids, a widely employed method to capture a first approximation of temperature/entropy components is the quasiharmonic method[15,28,45,46] (QHM), which uses the locally stable equilibrium geometry and takes lattice thermal expansion into account, but otherwise remains within the bounds of the harmonic approximation. While the quasiharmonic approximation does not account for all consequences of anharmonicity,[47] some of its limitations can potentially be mitigated. As a workflow, the QHM is computationally tractable and, additionally, naturally includes approximate (i.e., harmonic) nuclear quantum effects in the free energy. The QHM has

previously been successfully applied to $MAPbI_3$ to capture properties of the material itself (e.g., lattice parameters,[20,48] elastic moduli and phase transitions[20,28]).

We here assess the quality of several density functionals in combination with the QHM and a simple entropy correction to account for MA^+ cation orientational disorder (similar to a correction applied and validated previously by Saidi and Choi[20]) for a somewhat more challenging purpose, i.e., a chemical reaction equilibrium. Specifically, for $MAPbI_3$, we are in the fortunate position that a well established temperature-pressure equilibrium with its decomposition products is published.[14,34] Ciccioli *et al.*[14,34] determined the product gas pressures needed to bring the system into equilibrium as a function of temperature, using Knudsen Effusion Mass Loss (KEML) and Knudsen Effusion Mass Spectrometry (KEMS). Three candidate reactions were considered:[34]

$$(CH_3NH_3)PbI_3 \rightarrow PbI_2 + CH_3I + NH_3\,, \tag{1}$$

$$(CH_3NH_3)PbI_3 \rightarrow PbI_2 + CH_3NH_2 + HI\,, \tag{2}$$

$$(CH_3NH_3)PbI_3 \rightarrow PbI_2 + CH_3NH_3I\,. \tag{3}$$

Ciccioli *et al.* found that the pressure calculated from pathway (2) closely matched measurements of the $MAPbI_3$ system. In principle, the products of pathway (1) are more energetically favorable than those of pathway (2).[12,16,34,35] However, pathway (1) is kinetically hindered at moderate temperatures (326 – 407 K for the KEML and KEMS experiments[14]), allowing pathway (2) to dictate the equilibrium pressures in this temperature range. Therefore, pathway (2) will be considered the dominant mode of decomposition in the present work. We stress that our study thus focuses on the experimentally established thermodynamic equilibrium (2), i.e., the starting and end points of a decomposition reaction, but we do not make any claims regarding the numerous possible, detailed kinetic processes involved in the decomposition or formation of an experimental sample. The decomposition mechanism (2) is in line with the broader literature,[6,12,27,34] and others (though without the detailed anal-

ysis of Ciccioli *et al.*) also report typical $MAPbI_3$ decomposition temperatures in the range of 100°C (373 K).[8,49] It is worth noting that the equilibrium pressures associated with the gas-phase decomposition products for the equilibrium temperature range investigated by Ciccioli *et al.* are extremely low (approximately 10^{-2}–10^{-3} Pa) compared to typical laboratory gas pressures, indicating that the stability of $MAPbI_3$ based devices against decomposition might increase significantly even in a trace gas atmosphere of its prospective decomposition products.

Our analysis indicates that the QHM, coupled with the Heyd-Scuseria-Ernzerhof (HSE06) hybrid density functional,[50,51] the Tkatchenko-Scheffler (TS) dispersion correction[52] and the aforementioned entropy correction[20] reproduces the published experimental equilibrium remarkably well. Interestingly, already the harmonic approximation for fixed lattice parameters (i.e., without the QHM correction) captures the reaction equilibrium, with only small energy corrections from volume expansion in the QHM. This observation lays the foundation to use the same, tractable approach for other hybrid metal halide perovskite materials in the future.

Methods

Methodological choices

The way to perform a computational evaluation of pathway (2) for comparison with experiment is, in principle, straightforward. One must simply calculate the Gibbs free energies g_i of the reactants and products i and then, for any given temperature, find the pressure at which the energy difference between the reactants and products, Δg, is zero. Even if the product gases are initially trapped in a solid-solid interface, they may thermodynamically be considered to be in equilibrium with an external gas phase (especially for the anticipated long lifetimes of an encapsulated photovoltaic device), and therefore it is valid to treat the material as if it is in contact with a gas.

Several key decisions must be made for a practical first-principles computation of the

relevant Gibbs free energy differences and the resulting temperature-pressure equilibria:

(i) Selection of the underlying method to compute total energies (the potential energy surface), i.e., the density functional approximation and relativistic formalism methods to be applied. In general, the validity and limits of different methods are not *a priori* clear. Providing this validation for several functionals is one of the objectives of this paper. Specifically, we apply the Perdew-Burke-Ernzerhof (PBE) functional,[53] the PBE-based hybrid functional known as PBE0,[54] and the HSE06 hybrid functional.[50,51] In each case, we account for the energy associated with van der Waals type dispersion interactions using the pairwise Tkatchenko-Scheffler (TS) van der Waals correction.[52] Our choice of the TS approach is motivated by a significant body of experience with the TS method applied to HOIP materials in our group, showing that the TS method generally produces equilibrium geometries in good agreement with published experimental structures.[4,13,20,55–60] The supporting information of Ref. 55 also shows that predicted structure differences for $MAPbI_3$ between the TS method and a more sophisticated many-body dispersion approach[61] are insignificant. Finally, a simple, theoretically motivated reparameterization[62] of the atomic polarizability of Cs renders the TS method applicable to Cs-containing HOIP nanostructures as well.[63]

(ii) Selection of the method used to calculate the free energy components associated with temperature and entropy of the solid and gaseous species. As mentioned above, the QHM is here applied to $MAPbI_3$ and PbI_2. The free energies of the gases are calculated by the harmonic oscillator / rigid rotor model. Anharmonic corrections to the free energies of the molecular species could be incorporated by more complex workflows of their own and has been demonstrated, for example, by Piccini *et al.* for small alkanes in zeolites.[64,65] In contrast, our analysis relies initially on the QHM only. The relevant equations to assess the g_i in solids and gases using the harmonic approximation or variants thereof are well known and included in the Appendix to keep this paper self-contained. We then incorporate a simple configurational entropy estimate to account for the most likely orientations of the MA^+ cations, aiming to capture the zero-order entropy difference due to MA^+ orientational changes

between important phases of $MAPbI_3$ (specificially, the low-temperature orthorhombic phase and the high-temperature cubic phase).

The free energy calculations for the cubic phase of $MAPbI_3$ are based on a fully-relaxed (including unit cell) orthorhombic geometry. The geometry of the MA^+ cation dictates that a minimal unit of $MAPbI_3$ cannot be locally of cubic symmetry, unlike the spatial or thermal average of such a unit in a diffraction experiment. Rather, even the "cubic" phase of $MAPbI_3$ in a diffraction sense will still exhibit significant local lattice distortion and tilting of octahedra.[19,28,30,42] Even at temperatures in which $MAPbI_3$ exists in the cubic phase, the orthorhombic unit cell may therefore provide a better approximation of the instantaneously preferred configurations of the crystal on the nanoscale.

In our calculations, we neglect the pV term of the Gibbs free energy of either $MAPbI_3$ or PbI_2 since the partial pressures of the involved gases remain relatively low (<50 mPa[34]) We note that, in high-pressure experiments, this term would be important. The high-pressure physics of $MAPbI_3$ has also been studied in other works[15,66] but does not pertain to the specific decomposition equilibrium conditions considered here.

Correction for configurational entropy of $MAPbI_3$

The QHM is suitable for a first-order approximation of the thermodynamics of $MAPbI_3$, but it does not take into account the intrinsic disorder of the $MAPbI_3$ lattice. At moderate to high temperatures, the methylammonium ions within the lattice are capable of realigning or even tumbling, causing distortion of the lattice around them. This overall anharmonic motion is also intricately linked to the different phases exhibited by methylammonium lead halides at different temperatures, as, e.g., some of us have shown in other work,[44] comparing temperature-dependent high-resolution X-ray diffraction and spectroscopies to ab initio molecular dynamics derived structural expectation values in $MAPbBr_3$. In general, modeling this behavior adds considerable complexity to any numerical approach; molecular dynamics simulations have been used to characterize it,[20] but these are computationally intensive, and

may become prohibitive if one wishes to model the behavior of $MAPbI_3$ over a range of temperatures. The QHM is suitable for a first-order approximation of the thermodynamics of $MAPbI_3$, but it does not take into account the intrinsic disorder of the $MAPbI_3$ lattice. At moderate to high temperatures, the methylammonium ions within the lattice are capable of realigning or even tumbling, causing distortion of the lattice around them. This overall anharmonic motion is also intricately linked to the different phases exhibited by methylammonium lead halides at different temperatures, as, e.g., some of us have shown in other work,[44] comparing temperature-dependent high-resolution X-ray diffraction and spectroscopies to ab initio molecular dynamics derived structural expectation values in $MAPbBr_3$. In general, modeling this behavior adds considerable complexity to any numerical approach; molecular dynamics simulations have been used to characterize it,[20] but these are computationally intensive, and may become prohibitive if one wishes to model the behavior of $MAPbI_3$ over a range of temperatures. In other solid systems with internal rotational degrees of freedom (such as hydrocarbons in zeolite lattices),[64] accurate calculations of the free energies associated with these degrees of freedom can be made by mapping the rotational energy well of the free species and thus calculating its rotational partition function. For example, Piccini *et al.* quantify the net impact of the anharmonic contribution to the adsorption Gibbs free energy ΔG of an ethane molecule in a zeolite cavity to $\approx$0.12 eV at T=313 K.[64] However, this method is expected to be most accurate in systems where each rotating species is functionally isolated from the others, and may therefore be treated separately from them. Due to the proximity of the methylammonium ions in the $MAPbI_3$ lattice and the flexible nature of the surrounding structure, such a method may not be applicable.

We here adopt a simple entropy correction strategy that accounts for expected preferential orientations of $MAPbI_3$ as validated earlier through explicit molecular dynamic simulations by Saidi and Choi.[20] If each methylammonium ion is considered to be in one of several low-energy orientations (each with probability p_i), then one may formulate a straightforward

configurational entropy term from the random alignment of ions:

$$s_{config} = -k_B \cdot \sum_{i=1}^{N} p_i \cdot \ln(p_i). \tag{4}$$

Molecular dynamics simulations have shown that, in the cubic phase, there are six most probable orientations of the methylammonium ion in $MAPbI_3$.[30,41,43,67] For six equally-probable configurations per methylammonium ion (and, thus, per formula unit), the formula Eq. (4) simplifies to the following expression:

$$s_{config} = k_B \cdot \ln(6). \tag{5}$$

It is important to note that, by assigning a probability of 1/6 to each possible orientation of each methylammonium ion, we have made the assumption that the individual ions' orientations are uncorrelated with one another. Molecular dynamics simulations[68,69] suggest that the static correlations between the orientations of neighboring MA^+ ions are highly significant at low temperatures, but decrease greatly as temperature increases to 300 K and above. As such, we expect this method to systematically and significantly overestimate the configurational entropy at low temperatures, but it may be approximately accurate in the temperature range (300 – 400 K) considered here. At T=313 K, Eq. (5) yields Ts_{config}=0.05 eV. As expected, this value is somewhat lower than the ethane/zeolite estimate of 0.12 eV by Piccini *et al.*[64] Due to the charged and polar nature of the MA^+ ion, it is expected that the forces between the ion and the host lattice would be significantly stronger than those between the ethane molecule and the zeolite lattice. These forces restrict the motion of the MA^+ ion to the extent that a reduction of configurational entropy by a factor of $\sim$2 compared to the ethane/zeolite system is understandable.

Computational Details

The structures of $MAPbI_3$, PbI_2, methylamine (MAe, to distinguish the neutral species CH_3NH_2 from the MA cation $CH_3NH_3^+$) and HI were obtained by relaxing them with the FHI-aims code[70] using the PBE[53] generalized gradient approximation (GGA) functional with the TS van der Waals correction. FHI-aims is an all-electron code based on numeric atom-centered basis functions, an efficient, high-precision recipe for electronic structure calculations verified by numerous past benchmarks[71,72] and also validated in numerous studies of perovskites.[55–60] As an all-electron code, FHI-aims represents the potential near the nucleus without any shape approximations, i.e., pseudopotentials or projectors are not used. Specific numerical settings used, including k-space grids for solids, are summarized in an appendix "Computational Settings". For static total-energy calculations, we also obtained fully relaxed structures using the HSE06+TS and PBE0+TS hybrid functionals. In addition to the atomic coordinates, the lattice vectors of $MAPbI_3$ and PbI_2 were relaxed as well, except for the QHM related geometries, where fixed lattice parameters are necessary to simulate thermal expansion. Note that FHI-aims can perform both periodic and non-periodic calculations on equal footing and isolated molecules were thus treated non-periodically. Also, the algorithm used to relax structures[73] is robust even for complex, subtle hybrid organic-inorganic perovskite crystal structures and has been used in our group to validate detailed single-crystal X-ray refined structures.[59,60] The starting structure for $MAPbI_3$ was the computationally relaxed (PBE+TS) low-temperature orthorhombic unit cell of Ref. 55. PbI_2 is the DFT-relaxed version of the $P\bar{3}m1$ literature structure (the 2H polytype).[74] For DFT-PBE+TS calculations, k-space sampling was carried out using Γ-centered Monkhorst-Pack integration grids of 6×6×6 points for $MAPbI_3$ and 12×12×9 points for PbI_2. For hybrid DFT calculations (HSE06+TS and PBE0+TS), we used k-space grids of 4×4×4 points for $MAPbI_3$ and 10×10×8 points for PbI_2. The parameters for the HSE06 functional were set as suggested by Krukau *et al.*[75] (exchange mixing 0.25, screening parameter 0.11 inverse Bohr radii). Scalar-relativistic total energy calculations were calculated using the atomic

zero-order regular approximation as defined in Eqs. (55) and (56) of Ref. 70. Experimental and computationally relaxed lattice parameters are compared in Table 1 and are in close agreement with one another.

Table 1: Comparison of experimental lattice parameters of $MAPbI_3$ and PbI_2 with lattice parameters relaxed by DFT-PBE+TS, DFT-HSE06+TS and DFT-PBE0+TS.

	a	b	c
$MAPbI_3$ orthorhombic, exp., T=100 K[67]	8.8657	12.6293	8.5769
$MAPbI_3$ orthorhombic, DFT-PBE+TS	9.00	12.71	8.47
$MAPbI_3$ orthorhombic, DFT-HSE06+TS	8.96	12.68	8.47
$MAPbI_3$ orthorhombic, DFT-PBE0+TS	8.95	12.66	8.47
PbI_2, exp., room temperature[74]	4.55	4.55	6.979
PbI_2, exp., room temperature[76]	4.557	4.557	6.979
PbI_2, comp., DFT-PBE+TS	4.55	4.55	7.16
PbI_2, comp., DFT-HSE06+TS	4.56	4.56	7.09
PbI_2, comp., DFT-PBE0+TS	4.56	4.56	7.11

The harmonic vibrational free energies of the isolated molecular species MAe and HI were calculated using finite displacements of the nuclei of 0.0025 Å, using an existing script[77] implemented in the FHI-aims package, which also provides the rotational free energy contribution. The vibrational free energies of $MAPbI_3$ and PbI_2 were obtained using finite-difference phonon calculations as implemented in the PHONOPY package,[78] with an atomic displacement parameter of 0.02 Å. Due to the large number of individual first-principles calculations necessary to determine the free energies (especially for $MAPbI_3$) in the finite-difference based QHM approach, vibrational and phonon calculations were carried out using DFT-PBE+TS, which is computationally affordable for this task. For the HSE06+TS and PBE0+TS hybrid functionals, PBE+TS vibrational energy and entropy terms were used as fixed corrections.

In order to account for the thermal expansion of $MAPbI_3$ and PbI_2, the QHM was used. As mentioned above, for $MAPbI_3$, we use the molecular arrangement of the low-temperature orthorhombic phase as the most plausible short-range order pattern to apply the QHM and later apply an entropy correction term to account for configurational disorder. For the QHM, we scale the computationally relaxed orthorhombic lattice (Table 1) by uniform

factors, i.e., we model the volume expansion while keeping the cell fixed at the local cell shape known from the orthorhombic phase). We note that the computational orthorhombic cell's lattice parameters deviate from exactly equal lattice parameters by 2.8%. However, it is important to note that local fluctuations will always occur in the soft lattice of a halide perovskite and our simple scaling of the computationally determined unit cell is therefore a justifiable approximation of experimental reality within the confines of the QHM. At each volume probed for phonon calculations of $MAPbI_3$, all cell-internal atomic positions were fully relaxed. Volumetric scaling factors of 0.99 to 1.06 were used. The case of PbI_2 is somewhat more complicated, in that it has a hexagonal crystal structure with two non-equivalent axes. Therefore, we sampled free energy landscape over a two-dimensional grid of scaling factors of the two independent lattice parameters a and c. Specifically, a was scaled by length scaling factors (LFs) between 0.98 and 1.05. The overall unit cell volume V was scaled by a separate volume scaling factor (VF) between 0.99 and 1.1, defining the respective values for the c lattice parameters associated with probed each pair of (a, V). In Figure 1, the resulting grids of free-energy values are shown for three different temperatures considered for the QHM. As expected, the predicted volume and lattice spacing a increase with increasing temperature. The actual minimum free-energy values of a and V as a function of temperature were determined from a smooth bivariate spline interpolation of free-energy landscapes on (a, V) grids analogous to those displayed in Figure 1.

Results and Discussion

Internal energies

Using the total energies associated with the DFT-relaxed structures (no temperature or entropy corrections), decomposition energies of $MAPbI_3$ were calculated straightforwardly as

$$\Delta e = e(PbI_2) + e(HI) + e(CH_3NH_2) - e(MAPbI_3). \tag{6}$$

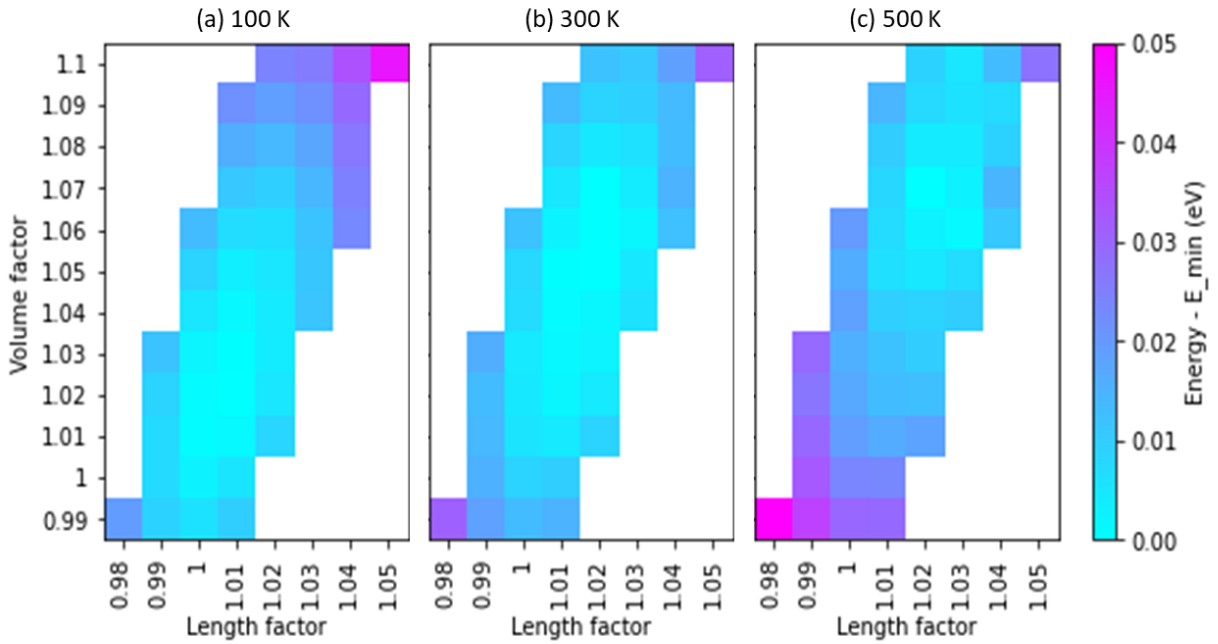

Figure 1: Gibbs free energy of PbI_2 at three representative temperatures at fixed volume and lattice parameter a in the harmonic approximation: (a) 100K, (b) 300K , and (c) 500K, plotted as a function of the in-plane length scaling factor (LF) and the volume scaling factor (VF). Energies are normalized by subtracting the minimum energy at each temperature.

The resulting Δe values for the three different density functionals are listed in Table 2. Clearly, $MAPbI_3$ is stable against decomposition absent vibrational energy and entropy corrections, consistent with its experimental stability at low temperature. The variation in predicted reaction energies between three different DFT methods is less than 0.1 eV per formula unit. The hybrid functionals (PBE0+TS and HSE06+TS) calculate a slightly higher (less favorable) internal energy change for the decomposition reaction than the PBE+TS functional does.

Gibbs free energies of solid and gaseous species

We next consider the impact of finite temperature and (for gaseous species) finite partial pressure contributions to the Gibbs free energy difference associated with reaction (2). Specifically, we consider the impact of phonons at varying unit cell volumes in the solid materials

Table 2: Total energy change Δe associated with the decomposition reaction Eq. (2) as calculated using each of three DFT methods, per $MAPbI_3$ formula unit (12 atoms). Note that the positive sign indicates that $MAPbI_3$ is stable against decomposition at the DFT total energy level.

Method	Reaction internal energy change (eV / formula unit)
PBE + TS	2.403
HSE06 + TS	2.487
PBE0 + TS	2.465

and vibrational, rotational and ideal-gas translational degrees of freedom for the molecular species in equilibrium with their gas phase, as summarized in the appendix (Eqs. (A.1–A.7)). The Gibbs free energy change of reaction varies with respect to three independent variables: temperature, total gas pressure p_{tot}, and the composition of the gas (fixed by the mole fraction of hydrogen iodide, x). Thus, in order to graph the equilibrium total pressure as a function of temperature, we must choose a value of x. While it would be sensible enough to choose $x = \frac{1}{2}$ as a default choice, this value is not optimal for the purposes of comparing our calculated pressures to experimental KEMS and KEML results, as the gas mixture inside a Knudsen cell is not equimolar, but is governed by the Knudsen effusion condition,[79,80] which is given in equation (7):

$$p_i = \frac{dm_i}{dt}\frac{1}{Af}\sqrt{\frac{2\pi k_B T}{M_i}}, \tag{7}$$

where p_i, M_i, and $\frac{dm_i}{dt}$ are the partial pressure, molecular weight, and mass effusion rate of species i, A is the area of the effusion orifice, and f is a geometric correction factor. We can reformulate equation (7) in terms of the particle effusion rate rather than the mass effusion rate ($\frac{dn_i}{dt} = \frac{1}{M_i}\frac{dm_i}{dt}$) and thus obtain

$$p_i = \frac{dn_i}{dt}\frac{1}{Af}\sqrt{2\pi k_B T M_i}. \tag{8}$$

Because each formula unit of $MAPbI_3$ decomposes into one molecule each of HI and MAe (in addition to the solid PbI_2), we know that the particle effusion rates of these species

are equal ($\frac{dn_{HI}}{dt} = \frac{dn_{MA}}{dt}$) when the Knudsen cell has reached a steady-state condition (i.e. neither gas is accumulating in the cell). As such, we may calculate the quotient of the partial pressures according to

$$\frac{p_{HI}}{p_{MA}} = \sqrt{\frac{M_{HI}}{M_{MA}}}, \tag{9}$$

which dictates the value of x as

$$x = \frac{p_{HI}}{p_{HI} + p_{MA}} = \left(1 + \sqrt{\frac{M_{MA}}{M_{HI}}}\right)^{-1} = \frac{\sqrt{M_{HI}}}{\sqrt{M_{HI}} + \sqrt{M_{MA}}} = 0.670. \tag{10}$$

The inclusion of the vibrational free energy contributions introduces a zero-point energy term. The zero-point energy for each reactant and product is reported in Table 3. The lattice parameters of $MAPbI_3$ and PbI_2 are kept fixed for this step of the analysis, i.e., quasiharmonic contributions related to thermal expansion are not yet included. The zero-point energy contributions disfavor the stability of $MAPbI_3$ by about 0.28 eV.

Table 3: Zero-point vibrational energy correction calculated for each species at the DFT-PBE+TS level of theory and using fixed lattice parameters (fully relaxed at the Born-Oppenheimer surface, i.e., not yet including any corrections due to finite temperature and/or the QHA), as well as the associated zero-point energy correction to the total reaction energy.

Species	Zero-point energy (eV / formula unit)
MA	1.689
HI	0.141
PbI_2	0.037
$MAPbI_3$	2.146
Reaction energy change	-0.279

In addition to zero-point energy corrections, finite-temperature free energy terms result from the vibrational/rotational and phonon calculations. These terms cause the decomposition products to be increasingly favored over $MAPbI_3$ as temperature increases. Figure 2 shows the reactant and product free energies vs. temperature, at four different, exemplary product gas pressures, this time also including the quasiharmonic terms for $MAPbI_3$ and

PbI_2. The point at which the reactant and product free energies cross, for a given gas pressure, represents equilibrium at that pressure. The equilibrium temperature depends on the partial pressures of the product gases due to the pressure dependence of the translational free energy of the gas. Above the equilibrium temperature, $MAPbI_3$ is unstable and is predicted to decompose. As seen in Figure 2, low product gas pressures correspond to low equilibrium temperatures, while high pressures result in high equilibrium temperatures. Figure 2 indicates that the equivalent product gas pressures associated with $MAPbI_3$ decomposition are indeed small (less than 0.1 Pa) around 400 K (the upper limit of the range investigated by Ciccioli *et al.*). Even modest counterpressures of the product gases MAe and HI would increase the decomposition temperature of $MAPbI_3$ by a substantial amount, far outside the anticipated operating temperatures of typical $MAPbI_3$ based devices.

Figure 2 also compares the change that results for the Gibbs free energy when including or excluding the entropy correction Eq. (5) that accounts approximately for MA^+ cationic configurational disorder. Although the difference appears small on the y-axis scale (several eV) plotted in Figure 2, it does cause a shift of the prospective equilibrium temperature to measurably higher values (around $\sim$10 K), as discussed in more detail further below.

Impact of the density functional approximation used

In the left panel of Figure 3, the equilibrium pressure of $MAPbI_3$ and its degradation products is plotted as a function of temperature, showing different computational approaches alongside the experimental data reported by Ciccioli *et al.*[14,34] This plot is the central result of the present work, since it allows us to directly compare the impact of different computational approximations on the accuracy of predicted temperature-pressure equilibria. As noted above, the DFT-PBE+TS approach including the entropy correction (blue dashed curve) yields higher equilibrium temperatures than without the entropy correction (blue solid curve), shifted by about 10 K. Although this shift is small, it is significant on the scale of the data of Ciccioli et al. The dashed blue curve (DFT-PBE+TS with entropy correction)

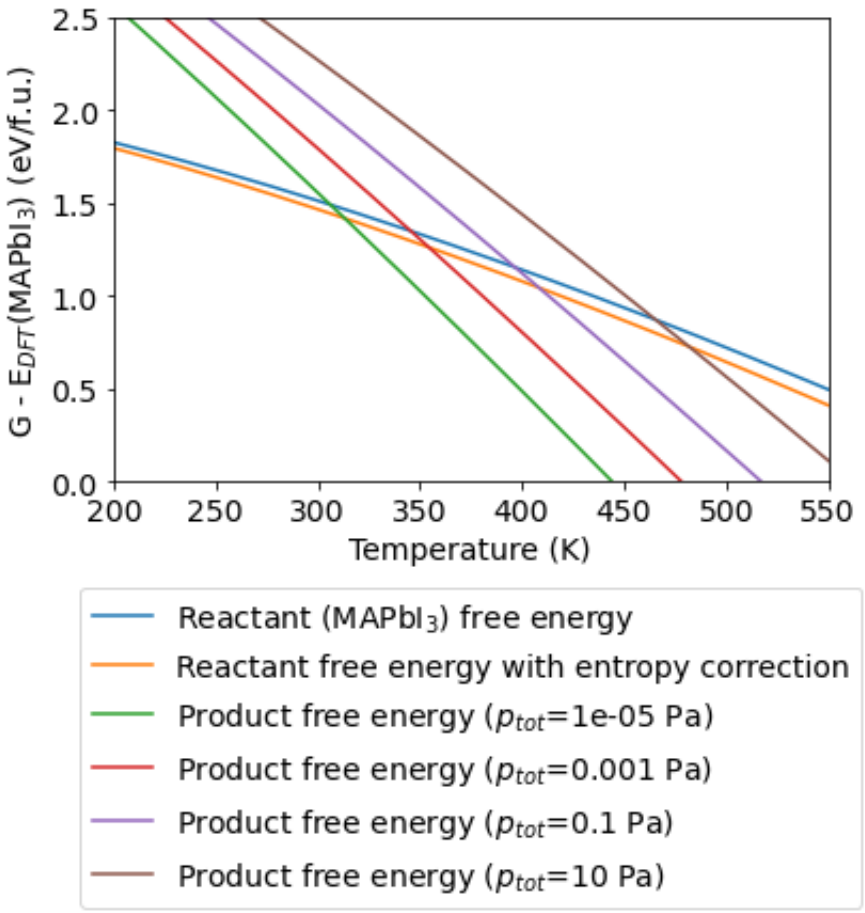

Figure 2: Gibbs free energy of $MAPbI_3$ (orange and blue curves, without and with entropy correction Eq. (5), respectively) and decomposition products vs temperature, at four selected pressures (green, red, purple, and brown curves, for p=10^{-5} Pa, 0.001 Pa, 0.1 Pa, and 10 Pa, respectively). The partial pressures of HI and MAe are chosen according to Eq. (10), and the reported pressure p is their sum. Free energies are defined in reference to the calculated DFT energy at the Born-Oppenheimer surface (E_{DFT}). All values are calculated using the DFT-PBE+TS level of theory.

is significantly closer to the experimental data than the solid curve without the entropy correction, but it still corresponds to equilibrium temperatures that are visibly underestimated (or, correspondingly, equilibrium partial pressures of the gaseous decomposition products HI and MAe that are visibly overestimated).

As described in the methods section, we considered the impact of two other density functionals (HSE06+TS and PBE0+TS) on the predicted temperature/pressure equilibrium. Specifically, we employed the total energies of the reactants and products for structures that

were fully relaxed at the target density functional, but kept the vibrational and rotational free energy corrections determined at the DFT-PBE+TS level of theory. Remarkably, either the HSE06+TS hybrid density functional or the PBE0+TS hybrid density functional produce predicted temperature/pressure equilibria that are almost precisely consistent with the experimental data, as long as the entropy correction is included. The original derivation of the PBE0 hybrid density functional does suggest a generally better performance of this functional than that of the simpler (and computationally cheaper) semilocal PBE density functional.[54,81] Similarly, the HSE06 density functional and its predecessors were originally derived with the aim of achieving similar accuracy to the PBE0 functional, but at anticipated lower cost of a short-range screened hybrid density functional.[50,51] It is therefore not surprising that the hybrid functionals yield somewhat improved thermodynamic predictions for the stability of $MAPbI_3$, compared to the simpler PBE+TS functional. In summary, our results suggest that using total energies and static structures derived from the hybrid PBE0+TS or HSE06+TS functionals, combined with quasiharmonic vibrational and rotational entropy corrections from the more affordable PBE+TS density functional, can yield accurate stability predictions for $MAPbI_3$. Given the general nature of the underlying approaches, we expect that this trend will also hold for hybrid organic-inorganic perovskites beyond $MAPbI_3$, the case for which detailed experimental reference data are available.

Impact of the Quasi-Harmonic Correction

A final point concerns the impact of the QHM. As mentioned above, this approximation allows one to predict temperature-dependent unit cell volumes and, thus, relaxes the restriction of free-energy calculations to a fixed unit cell. The underlying free energy is, however, still computed in the harmonic approximation, since anharmonic motion of the atoms themselves is not accounted for. For the purposes of this paper, the most important role of the QHM is the overall correction that it imparts to the free energies of the solids in Eq. (2) and, thus, to the calculated temperature-pressure equilibrium curve of $MAPbI_3$ decomposition. As a

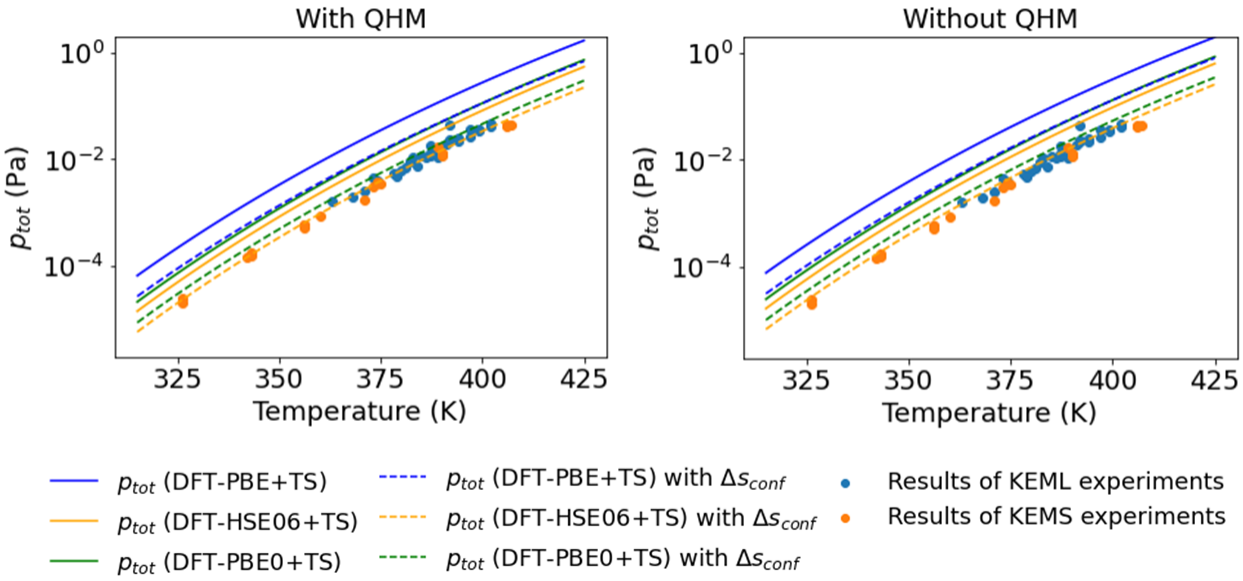

Figure 3: Equilibrium total pressure vs. temperature, for various DFT methods, including harmonic contributions with and without considering the volume expansion of the solid phases (labeled "with QHM" and "without QHM", respectively). The graphs look nearly identical, illustrating the relatively minor role of the volume-dependent terms for the temperature-pressure equilibrium with the gas phase species. For the calculated and KEML results, the partial pressure ratio was determined by Eq. (10). For the KEMS results, the partial pressures are measured independently, so no such assumption is necessary. KEML and KEMS results were taken from ref. 14.

second result, however, one can also derive the QHM-corrected unit cell volumes themselves, albeit leaving out true anharmonic effects, such as molecular rotation. For example, Saidi and Choi[20] used the QHM for this purpose for $MAPbI_3$.

Figure 4 compares different temperature-dependent experimental and computational results for the unit cell volumes of $MAPbI_3$ (Figure 4a) and PbI_2 (Figure 4b). Commenting on PbI_2 first, there is a practically constant offset between the computational and experimental data, but the trend with temperature is otherwise identical within the temperature range covered by the experimental literature data shown in Fig 4. The offset of a few percent between the DFT-PBE+TS data and the experiments is within the range that is typical of experiment-computation discrepancies for unit cell volumes and the temperature trend is essentially the same. The situation for $MAPbI_3$ is more complex and likely indicative of the limits of the QHM for anharmonic structural degrees of freedom. In the low-temperature

(orthorhombic) regime below ∼160 K, the slope of the computational and experimental volumes as a function of temperature agrees. The experimental data are only separated from the computational data by different constant offsets, as in the case of PbI_2. The offset between our computational results and those of Saidi and Choi[20] is also constant and attributed to different density functionals used (DFT-PBE+TS here vs. DFT-PBEsol by Saidi and Choi). The trend of the computational data is otherwise nearly exactly the same over the entire temperature range plotted. In contrast, the experimental unit cell volume experiences a discontinuous change at the orthorhombic-tetragonal phase transition at ∼160 K. This change cannot be captured by the QHM and is likely associated with a freeing-up of the molecular conformation to a larger ensemble in which the molecules can rotate.[44] This is the very rotation that, for the Gibbs free energy, we (as well as by Saidi and Choi) capture via the qualitative entropy term of Eq. (5), but which does not enter the QHM unit cell volume determination. As expected, volume changes above the phase transition temperature of ∼160 K can therefore not be captured in their entirety by the QHM alone.

Interestingly, and as shown in Table 4, the actual QHM energy contributions (i.e., those contributions that are not already captured as harmonic terms and which are genuinely attributable to the volume expansion) only make a minute difference to the actual free energy differences of relevance in the thermodynamic temperature-pressure equilibrium between $MAPbI_3$ and its decomposition products in Eq. (2). The overall energy scale of Gibbs free energies in Figure 2 is of the order of several eV, whereas the energy changes due to the QHM in Table 4 are roughly two orders of magnitude smaller. In fact, the entropy correction in Eq. (5) itself is larger than the overall QHM correction, making this term the more important one compared to the volume-change related energy differences. Thus, even the simple harmonic approximation at static volumes together with the configurational entropy correction would, according to our results, have captured the majority of the contribution necessary to predict the temperature-pressure stability equilibrium of Figure 3. The right panel of Figure 3, which omits the effect of volume expansion, shows that the resulting

changes are very small.

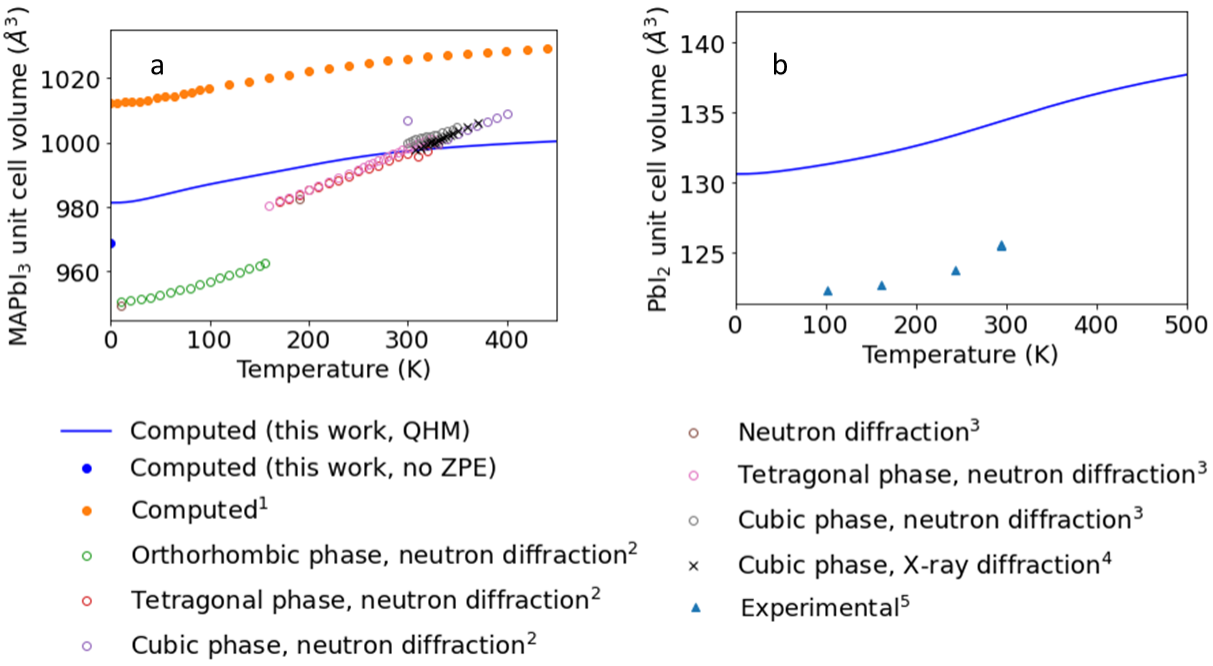

Figure 4: Calculated (DFT-PBE+TS with QHM) and experimental unit cell volumes for $MAPbI_3$ and PbI_2. (a) $MAPbI_3$ cell volume vs temperature. (b) PbI_2 cell volume vs temperature. (1) Data from Ref. 20. (2) Data from Ref. 55. (3) Data from Ref. 82. (4) Data from Ref. 83. (5) Data from Refs. 76, 84, 85.

Table 4: QHM free energy corrections per formula unit for $MAPbI_3$ and PbI_2 at various temperatures, along with the resulting reaction energy correction.

Temperature (K)	$MAPbI_3$ QHM free energy correction (eV)	PbI_2 QHM free energy correction (eV)	Reaction QHM free energy correction (eV)
300	-0.0178	-0.0092	0.0086
350	-0.0216	-0.0118	0.0098
400	-0.0255	-0.0149	0.0106
450	-0.0294	-0.0184	0.0111
500	-0.0340	-0.0221	0.0119

Conclusion

In this work, we demonstrate that applying a set of computationally affordable models to the thermodynamic stability limits of the paradigmatic hybrid organic-inorganic semiconductor $MAPbI_3$ can model temperature-pressure equilibrium data in close agreement with experimental reference data. Specifically, remarkably good accuracy is achieved when using (i) total energies for static structures predicted at the level of the dispersion corrected hybrid density functionals PBE0+TS or HSE06+TS, (ii) harmonic free-energy corrections for gaseous and solid species at the more affordable, dispersion corrected semilocal DFT-PBE+TS level of theory, (iii) the low-temperature local order of molecular species in the orthorhombic phase of $MAPbI_3$ to approximate residual short-range order, combined with a simple entropy correction to account for molecular orientational degrees of freedom and (iv) quasiharmonic corrections to account for thermal expansion effects. In contrast, just using the computationally cheaper PBE+TS approximation for (i), i.e., the internal energies, would not produce the same quality of computational results. Although still more expensive than semilocal DFT calculations such as PBE, hybrid DFT calculations can now be carried out with affordable efficiency and with high precision up to very large system sizes, e.g., up to 3,383 atoms in a perovskite structure in Ref. 86. Interestingly, the quasiharmonic corrections (while important to predict qualitatively correct volume expansion trends for the low-temperature phase) do not appear to impact the overall predicted temperature-pressure equilibria of $MAPbI_3$ and its decomposition products strongly. We have thus validated a computational approach that is expected to be helpful to predict thermodynamic stability criteria for the much larger space of other hybrid organic-inorganic semiconductors, although we note that any necessary qualitative entropy corrections for molecular rotations will be system-dependent (e.g., depend on the number and freedom of molecular rotors present). Importantly, the underlying reaction equilibria also offer an approach to actively stabilize these materials against decomposition by offering reactants such as methylamine, HI and I_2 at sufficiently high partial pressures to establish or re-establish appropriate thermodynamic

equilibrium conditions that stabilize the hybrid perovskite in operando.

Acknowledgement

This work was supported by NSF Award number DMR-1729297. D.H. acknowledges a research experience for undergraduates (REU) fellowship "Meeting the Grand Challenges in Engineering" at Duke University under NSF award number 1659615. This work was supported in part through computational resources and services provided by the Institute for Cyber-Enabled Research at Michigan State University. The authors are grateful to Dr. Raul Laasner for mentorship of D.H. during his REU stay at Duke University in 2019.

Data Availability

Material structures and computational parameters used for the calculations in this work may be downloaded from DOI https://doi.org/10.6084/m9.figshare.22770668.

Appendix: Thermodynamic Formalism

Although the formalism to compute thermodynamic equilibria between solids and gaseous species is well established in physical chemistry, we here summarize the full formalism to identify all of the specific choices made in the present work. Importantly, our results ultimately connect to the total pressure measured in a KEMS or KEML experiment, which is not always the target property in a textbook derivation. The total pressure, p_{tot} of the decomposition gas mixture in equilibrium with the solid phases is the main formula derived in this appendix.

The Gibbs free energy change associated with the decomposition of one formula unit of

$MAPbI_3$ according to (2) is given by Eq. (A.1):

$$\Delta g = g_{PbI2} + g_{HI} + g_{MAe} - T \cdot \Delta s_{\text{mix}} - g_{MAPbI3}. \tag{A.1}$$

Here, g_i denotes the Gibbs free energy per formula unit of each component i (solid or gaseous) involved in the reaction equilibrium. Additionally, we consider the entropy of mixing per gas molecule of the gaseous species, Δs_{mix} (see below), assuming equilibrium with a mixed-gas atmosphere. For each of the solid species ($MAPbI_3$ and PbI_2), g_i is expressed as a sum of the internal energy at a T=0 K (e_0) and an additional free energy term which captures the vibrational free energy of the solid (f_{vib}). The pressure-volume term of the free energy is negligible at the relatively low pressures considered here, so the f_{vib} term is considered to be a function of temperature but not pressure. For the gaseous species, g_i is expressed as a sum of the internal energy at T=0 K (e_0), the translational free energy of the gas (f_{trans}), and the rotational and vibrational free energies, which are combined into the term (f_{rv}).[87] f_{trans} is a function of both temperature and pressure, and f_{rv} is a function of only temperature:

$$\begin{aligned}\Delta g = {} & e_{0,PbI2} + f_{PbI2}(T) + e_{0,HI} + f_{trans,HI}(T,p) + f_{rv,HI}(T) + \\ & e_{0,MAe} + f_{trans,MAe}(T,p) + f_{rv,MAe}(T) - T \cdot \Delta s_{\text{mix}} - e_{0,MAPbI3} - f_{MAPbI3}(T).\end{aligned} \tag{A.2}$$

In order to solve Eq. (A.2) for equilibrium pressure, the pressure-dependent translational free energy terms may be isolated and written out as:

$$f_{trans,HI} + f_{trans,MAe} = k_B T \left[\ln\left(\left(\frac{M_{HI} k_B T}{2\pi\hbar^2} \right)^{3/2} \frac{k_B T}{p_{HI}} \right) + \ln\left(\left(\frac{M_{MAe} k_B T}{2\pi\hbar^2} \right)^{3/2} \frac{k_B T}{p_{MAe}} \right) \right], \tag{A.3}$$

such that

$$k_BT\left[\ln\left(\left(\frac{M_{HI}k_BT}{2\pi\hbar^2}\right)^{3/2}\frac{k_BT}{p_{HI}}\right)+\ln\left(\left(\frac{M_{MAe}k_BT}{2\pi\hbar^2}\right)^{3/2}\frac{k_BT}{p_{MAe}}\right)\right]= \\ e_{0,MAPbI3}+f_{MAPbI3}(T)-e_{0,PbI2}-f_{PbI2}(T) \\ -e_{0,HI}-f_{rv,HI}(T)-e_{0,MAe}-f_{rv,MAe}(T)+T\cdot\Delta s_{\text{mix}}. \quad \text{(A.4)}$$

It is convenient to consolidate the right-hand side of Eq. (A.4) into a single term, denoted Σe:

$$\Sigma e = e_{0,MAPbI3}+f_{MAPbI3}(T)-e_{0,PbI2}-f_{PbI2}(T)-e_{0,HI}-f_{rv,HI}(T)-e_{0,MAe}-f_{rv,MAe}(T)+T\cdot\Delta s_{\text{mix}}. \quad \text{(A.5)}$$

Substituting Σe into Eq. (A.4) allows for the isolation of the pressure-dependent term:

$$\ln\left(\frac{M_{HI}^{3/2}M_{MAe}^{3/2}k_B^5T^5}{8\pi^3\hbar^6p_{HI}p_{MAe}}\right)=\frac{\Sigma e}{k_BT} \quad\Longrightarrow\quad \frac{M_{HI}^{3/2}M_{MAe}^{3/2}k_B^5T^5}{8\pi^3\hbar^6p_{HI}p_{MAe}}=\exp\left(\frac{\Sigma e}{k_BT}\right) \quad \text{(A.6)}$$

or

$$p_{HI}p_{MAe}=\frac{M_{HI}^{3/2}M_{MAe}^{3/2}k_B^5T^5}{8\pi^3\hbar^6}\exp\left(-\frac{\Sigma e}{k_BT}\right). \quad \text{(A.7)}$$

In the case of a mixture of n_{HI} and n_{MAe} particles of HI and MAe, respectively, where x, the mole fraction of HI, is given by $x = n_{HI}/(n_{HI}+n_{MAe})$, statistical mechanics[87] gives the entropy of mixing as follows:

$$S_{\text{mix}} = -k_B(n_{HI}\cdot\ln(x)+n_{MAe}\cdot\ln(1-x)). \quad \text{(A.8)}$$

The Δs_{mix} of Eq. (A.5) is not the entropy given by Eq. (A.8) (the total entropy of mixing of the gas mixture), but rather the incremental entropy of mixing associated with releasing one molecule each of HI and MAe into the mixed-gas phase. Its value is calculated according

to

$$\Delta s_{\text{mix}} = \frac{\partial S_{\text{mix}}}{\partial n_{HI}} \Delta n_{HI} + \frac{\partial S_{\text{mix}}}{\partial n_{MAe}} \Delta n_{MAe} = \bar{s}_{HI} \Delta n_{HI} + \bar{s}_{MAe} \Delta n_{MAe}, \tag{A.9}$$

where $\Delta n_{HI} = \Delta n_{MAe} = 1$ refer to the number of molecules of HI and MAe released per formula unit of $MAPbI_3$ decomposed. $\bar{s}_{HI}$ and $\bar{s}_{MAe}$ are the partial molecular entropies of HI and MAe, which can be found by taking partial derivatives of the entropy of mixing of Eq. (A.8):

$$\bar{s}_{HI} = \frac{\partial S_{\text{mix}}}{\partial n_{HI}} \tag{A.10}$$

$$\bar{s}_{MAe} = \frac{\partial S_{\text{mix}}}{\partial n_{MAe}} \tag{A.11}$$

To take these derivatives, we express Eq. (A.8) in terms of n_{HI} and n_{MAe} rather than in terms of N and x, where x is the mole fraction of HI:

$$S_{\text{mix}} = -\big(n_{HI} + n_{MAe}\big) k_B \left(\frac{n_{HI}}{n_{HI} + n_{MAe}} \cdot \ln \frac{n_{HI}}{n_{HI} + n_{MAe}} + \frac{n_{MAe}}{n_{HI} + n_{MAe}} \cdot \ln \frac{n_{MAe}}{n_{HI} + n_{MAe}} \right), \tag{A.12}$$

$$S_{\text{mix}} = -k_B (n_{HI} \ln \frac{n_{HI}}{n_{HI} + n_{MAe}} + n_{MAe} \ln \frac{n_{MAe}}{n_{HI} + n_{MAe}}). \tag{A.13}$$

Now, we differentiate with respect to n_{HI} to find $\bar{s}_{HI}$:

$$\bar{s}_{HI} = -k_B \Bigg[\ln \frac{n_{HI}}{n_{HI} + n_{MAe}} + n_{HI} \frac{n_{HI}}{n_{HI} + n_{MAe}} \left(\frac{1}{n_{HI} + n_{MAe}} - \frac{n_{HI}}{(n_{HI} + n_{MAe})^2} \right) + n_{MAe} \frac{n_{HI} + n_{MAe}}{n_{MAe}} \frac{-n_{MAe}}{(n_{HI} + n_{MAe})^2} \Bigg], \tag{A.14}$$

$$\bar{s}_{HI} = -k_B \left[\ln \frac{n_{HI}}{n_{HI} + n_{MAe}} + \left(1 - \frac{n_{HI}}{n_{HI} + n_{MAe}} \right) - \frac{n_{MAe}}{n_{HI} + n_{MAe}} \right] = -k_B \ln \frac{n_{HI}}{n_{HI} + n_{MAe}}. \tag{A.15}$$

When this process is repeated, but the derivative is taken with respect to n_{MAe}, to find $\bar{s}_{MAe}$, a similar result is found:

$$\bar{s}_{MAe} = -k_B \ln \frac{n_{MAe}}{n_{HI} + n_{MAe}}. \tag{A.16}$$

Now that we have found the formulas for $\bar{s}_{HI}$ and $\bar{s}_{MAe}$, we may substitute x and $1 - x$ (the

mole fractions of HI and MAe) for $n_{HI}/(n_{HI}+n_{MAe})$ and $n_{MAe}/(n_{HI}+n_{MAe})$:

$$\bar{s}_{HI} = -k_B \ln x, \tag{A.17}$$

$$\bar{s}_{MAe} = -k_B \ln (1-x). \tag{A.18}$$

These formulas for the partial molar entropies of HI and MAe may now be substituted into Eq. (A.9) to find the entropy of mixing per formula unit of reaction Δs_{mix}:

$$\Delta s_{\mathrm{mix}} = -k_B(\ln x + \ln (1-x)) \tag{A.19}$$

For any given gas composition, Eq. (A.19) allows the calculation of Σe (which is now a function of both temperature and composition) according to Eq. (A.5). Also, because the ratio of partial pressures in an ideal gas mixture equals the molar ratio between the constituent gases,

$$p_{HI} = p_{\mathrm{tot}} x, \tag{A.20}$$

$$p_{MAe} = p_{\mathrm{tot}} (1-x). \tag{A.21}$$

Substituting Eqs. (A.20), (A.21) into equation (A.7) results in a formula for the total equilibrium pressure for any gas composition x:

$$p_{\mathrm{tot}} = \sqrt{\frac{1}{x(1-x)} \frac{m_{HI}^{3/2} m_{MAe}^{3/2} k_B^5 T^5}{8\pi^3 \hbar^6}} \exp\left(-\frac{\Sigma e}{2k_B T}\right) \tag{A.22}$$

Appendix: Computational Settings

Numerical settings for all DFT calculations are summarized in Table A.1.

Table A.1: Computational settings used for DFT calculations reported in this work, where "numerical settings" summarizes pre-tabulated basis sets and numerical choices provided with the FHI-aims code. "XC" stands for the exchange-correlation functional used.

Calculation	XC	Numerical settings	k-grid
Relaxations			
$MAPbI_3$	PBE+TS	Tight	6×6×6
PbI_2	PBE+TS	Tight	12×12×9
MAe	PBE+TS	Tight	
HI	PBE+TS	Tight	
QHM (phonon) calculations			
$MAPbI_3$	PBE+TS	Tight	6×6×6
PbI_2	PBE+TS	Tight	12×12×9
Molecular vibrational calculations			
MAe	PBE+TS	Tight	
HI	PBE+TS	Tight	
PBE0 single-point calculations			
$MAPbI_3$	PBE0+TS	Intermediate	4×4×4
PbI_2	PBE0+TS	Intermediate	10×10×8
MAe	PBE0+TS	Intermediate	
HI	PBE0+TS	Intermediate	
HSE06 single-point calculations			
$MAPbI_3$	HSE06+TS	Intermediate	4×4×4
PbI_2	HSE06+TS	Intermediate	10×10×8
MAe	HSE06+TS	Intermediate	
HI	HSE06+TS	Intermediate	

References

(1) Wong-Stringer, M.; Game, O. S.; Smith, J. A.; Routledge, T. J.; Alqurashy, B. A.; Freestone, B. G.; Parnell, A. J.; Vaenas, N.; Kumar, V.; Alawad, M. O. A.; Iraqi, A.; Rodenburg, C.; Lidzey, D. G. High-Performance Multilayer Encapsulation for Perovskite Photovoltaics. *Advanced Energy Materials* **2018**, *8*, 1801234.

(2) Zhou, Y.; Yin, Y.; Zuo, X.; Wang, L.; Li, T.-D.; Xue, Y.; Subramanian, A.; Fang, Y.; Guo, Y.; Yang, Z.; Cotlet, M.; Nam, C.-Y.; Rafailovich, M. H. Improving Thermal Stability of Perovskite Solar Cells by Suppressing Ion Migration Using Copolymer Grain Encapsulation. *Chemistry of Materials* **2021**, *33*, 6120–6135.

(3) Raman, R. K.; Gurusamy Thangavelu, S. A.; Venkataraj, S.; Krishnamoorthy, A. Materials, methods and strategies for encapsulation of perovskite solar cells: From past to present. *Renewable and Sustainable Energy Reviews* **2021**, *151*, 111608.

(4) Balestra, S. R. G.; Vicent-Luna, J. M.; Calero, S.; Tao, S.; Anta, J. A. Efficient modelling of ion structure and dynamics in inorganic metal halide perovskites. *J. Mater. Chem. A* **2020**, *8*, 11824–11836.

(5) Li, J.; Xia, R.; Qi, W.; Zhou, X.; Cheng, J.; Chen, Y.; Hou, G.; Ding, Y.; Li, Y.; Zhao, Y.; Zhang, X. Encapsulation of perovskite solar cells for enhanced stability: Structures, materials and characterization. *Journal of Power Sources* **2021**, *485*, 229313.

(6) Shi, L.; Bucknall, M. P.; Young, T. L.; Zhang, M.; Hu, L.; Bing, J.; Lee, D. S.; Kim, J.; Wu, T.; Takamure, N.; McKenzie, D. R.; Huang, S.; Green, M. A.; Ho-Baillie, A. W. Y. Gas chromatography–mass spectrometry analyses of encapsulated stable perovskite solar cells. *Science* **2020**, *368*, eaba2412.

(7) Wang, R.; Mujahid, M.; Duan, Y.; Wang, Z.-K.; Xue, J.; Yang, Y. A Review of Perovskites Solar Cell Stability. *Advanced Functional Materials* **2019**, *29*, 1808843.

(8) Philippe, B.; Park, B.-W.; Lindblad, R.; Oscarsson, J.; Ahmadi, S.; Johansson, E. M. J.; Rensmo, H. Chemical and Electronic Structure Characterization of Lead Halide Perovskites and Stability Behavior under Different Exposures—A Photoelectron Spectroscopy Investigation. *Chemistry of Materials* **2015**, *27*, 1720–1731.

(9) Li, J.; Bouchard, M.; Reiss, P.; Aldakov, D.; Pouget, S.; Demadrille, R.; Aumaitre, C.; Frick, B.; Djurado, D.; Rossi, M.; Rinke, P. Activation Energy of Organic Cation Rotation in CH3NH3PbI3 and CD3NH3PbI3: Quasi-Elastic Neutron Scattering Measurements and First-Principles Analysis Including Nuclear Quantum Effects. *The Journal of Physical Chemistry Letters* **2018**, *9*, 3969–3977, PMID: 29961330.

(10) Nazeeruddin, M.; Snaith, H. Methylammonium lead triiodide perovskite solar cells: A new paradigm in photovoltaics. *MRS Bulletin* **2015**, *40*, 641–645.

(11) Fan, Y.; Qin, H.; Ye, W.; Liu, M.; Huang, F.; Zhong, D. Improving the stability of methylammonium lead iodide perovskite solar cells by cesium doping. *Thin Solid Films* **2018**, *667*, 40–47.

(12) Alessandro Latini, G. G.; Ciccioli, A. A study on the nature of the thermal decomposition of methylammonium lead iodide perovskite, CH3NH3PbI3: an attempt to rationalise contradictory experimental results. *Sustainable Energy Fuels* **2017**, *1*, 1351–1357.

(13) Zhang, Y.-Y.; Chen, S.; Xu, P.; Xiang, H.; Gong, X.-G.; Walsh, A.; Wei, S.-H. Intrinsic Instability of the Hybrid Halide Perovskite Semiconductor CH3NH3PbI3. *Chinese Physics Letters* **2018**, *35*, 1–7.

(14) Brunetti, B.; Cavallo, C.; Ciccioli, A. On the Thermal and Thermodynamic (In)Stability of Methylammonium Lead Halide Perovskites. *Sci Rep* **2016**, *6*, 31896.

(15) Ke, F.; Wang, C.; Jia, C.; Wolf, N.; Yan, J.; Niu, S.; Devereaux, T.; Karunadasa, H.; Mao, W.; Lin, Y. Preserving a robust CsPbI3 perovskite phase via pressure-directed octahedral tilt. *Nat. Commun.* **2021**, *12*, 461.

(16) Akbulatov, A. F.; Martynenko, V. M.; Frolova, L. A.; Dremova, N. N.; Zhidkov, I.; Tsarev, S. A.; Luchkin, S. Y.; Kurmaev, E. Z.; Aldoshin, S. M.; Stevenson, K. J.; Troshin, P. A. Intrinsic thermal decomposition pathways of lead halide perovskites APbX3. *Solar Energy Materials and Solar Cells* **2020**, *213*, 110559.

(17) Nagabhushana, G. P.; Shivaramaiah, R.; Navrotsky, A. Direct calorimetric verification of thermodynamic instability of lead halide hybrid perovskites. *Proceedings of the National Academy of Sciences* **2016**, *113*, 7717–7721.

(18) Kim, N.-K.; Min, Y. H.; Noh, S.; Cho, E.; Jeong, G.; Joo, M.; Ahn, S.-W.; Lee, J. S.; Kim, S.; Ihm, K.; Ahn, H.; Kang, Y.; Lee, H.-S.; Kim, D. Investigation of Thermally Induced Degradation in CH3NH3PbI3 Perovskite Solar Cells using In-situ Synchrotron Radiation Analysis. *Scientific Reports* **2017**, *7*, 2045–2322.

(19) Beecher, A. N.; Semonin, O. E.; Skelton, J. M.; Frost, J. M.; Terban, M. W.; Zhai, H.; Alatas, A.; Owen, J. S.; Walsh, A.; Billinge, S. J. L. Direct Observation of Dynamic Symmetry Breaking above Room Temperature in Methylammonium Lead Iodide Perovskite. *ACS Energy Letters* **2016**, *1*, 880–887.

(20) Saidi, W. A.; Choi, J. J. Nature of the cubic to tetragonal phase transition in methylammonium lead iodide perovskite. *The Journal of chemical physics* **2016**, *145 14*, 144702.

(21) Zhao, Y. et al. A bilayer conducting polymer structure for planar perovskite solar cells with over 1,400 hours operational stability at elevated temperatures. *Nature Energy* **2022**, *7 2*, 144–152.

(22) Milić, J. V.; Zakeeruddin, S. M.; Grätzel, M. Layered Hybrid Formamidinium Lead Iodide Perovskites: Challenges and Opportunities. *Accounts of Chemical Research* **2021**, *54*, 2729–2740, PMID: 34085817.

(23) Hoye, R. L. Z.; Brandt, R. E.; Osherov, A.; Stevanović, V.; Stranks, S. D.; Wilson, M. W. B.; Kim, H.; Akey, A. J.; Perkins, J. D.; Kurchin, R. C.; Poindexter, J. R.; Wang, E. N.; Bawendi, M. G.; Bulović, V.; Buonassisi, T. Methylammonium Bismuth Iodide as a Lead-Free, Stable Hybrid Organic–Inorganic Solar Absorber. *Chemistry – A European Journal* **2016**, *22*, 2605–2610.

(24) Wang, T.; Wei, Q.; Fu, Q.; Li, W.; Wang, S.-W. Review of Perovskite Photovoltaic Cell Encapsulation Material and Technology. *Chinese Journal of Applied Chemistry* **2022**, *39*, 1321 – 1344, Cited by: 0.

(25) Min, H.; Lee, D. Y.; Kim, J.; Kim, G.; Lee, K. S.; Kim, J.; Paik, M. J.; Kim, Y. K.; Kim, K. S.; Kim, M. G.; Shin, T. J.; Il Seok, S. Perovskite solar cells with atomically coherent interlayers on SnO2 electrodes. *Nature* **2021**, *598*, 444–450.

(26) Wang, M.; Fei, C.; Uddin, M. A.; Huang, J. Influence of voids on the thermal and light stability of perovskite solar cells. *Science Advances* **2022**, *8*, eabo5977.

(27) Myung, C. W.; Hajibabaei, A.; Cha, J.-H.; Ha, M.; Kim, J.; Kim, K. S. Challenges, Opportunities, and Prospects in Metal Halide Perovskites from Theoretical and Machine Learning Perspectives. *Advanced Energy Materials* **2022**, 2202279.

(28) Carignano, M. A.; Aravindh, S. A.; Roqan, I. S.; Even, J.; Katan, C. Critical Fluctuations and Anharmonicity in Lead Iodide Perovskites from Molecular Dynamics Supercell Simulations. *The Journal of Physical Chemistry C* **2017**, *121*, 20729–20738.

(29) Toloueinia, P.; Khassaf, H.; Shirazi Amin, A.; Tobin, Z. M.; Alpay, S. P.; Suib, S. L. Moisture-Induced Structural Degradation in Methylammonium Lead Iodide Perovskite Thin Films. *ACS Applied Energy Materials* **2020**, *3*, 8240–8248.

(30) Bechtel, J. S.; Seshadri, R.; Van der Ven, A. Energy Landscape of Molecular Motion in Cubic Methylammonium Lead Iodide from First-Principles. *The Journal of Physical Chemistry C* **2016**, *120*, 12403–12410.

(31) Peng, W.; Mao, K.; Cai, F.; Meng, H.; Zhu, Z.; Li, T.; Yuan, S.; Xu, Z.; Feng, X.; Xu, J.; McGehee, M. D.; Xu, J. Reducing nonradiative recombination in perovskite solar cells with a porous insulator contact. *Science* **2023**, *379*, 683–690.

(32) National Renewable Energy Laboratory Best Research-Cell Efficiency Chart, Rev. 07-10-2023. `https://www.nrel.gov/pv/cell-efficiency.html`.

(33) Wolff, C. M. 2022; Private communication.

(34) Ciccioli, A.; Latini, A. Thermodynamics and the Intrinsic Stability of Lead Halide Perovskites CH3NH3PbX3. *J. Am. Chem. Soc.* **2018**, *9*, 3756–3765.

(35) Juarez-Perez, E.; Ono, L.; Maeda, M.; Jiang, Y.; Hawash, Z.; Qi, Y. Photodecomposition and Thermal Decomposition in Methylammonium Halide Lead Perovskites and Inferred Design Principles to Increase Photovoltaic Device Stability. *J. Mater. Chem. A* **2018**, *6*, 9604–9612.

(36) Mitzi, D.; Liang, K. Synthesis, Resistivity, and Thermal Properties of the Cubic Perovskite $NH_2CH{=}NH_2SnI_3$ and Related Systems. *Journal of Solid State Chemistry* **1997**, *134*, 376–381.

(37) Eperon, G. E.; Stranks, S. D.; Menelaou, C.; Johnston, M. B.; Herz, L. M.; Snaith, H. J. Formamidinium lead trihalide: a broadly tunable perovskite for efficient planar heterojunction solar cells. *Energy Environ. Sci.* **2014**, *7*, 982–988.

(38) Li, Z.; Yang, M.; Park, J.-S.; Wei, S.-H.; Berry, J. J.; Zhu, K. Stabilizing Perovskite Structures by Tuning Tolerance Factor: Formation of Formamidinium and Cesium Lead Iodide Solid-State Alloys. *Chemistry of Materials* **2016**, *28*, 284–292.

(39) Kulbak, M.; Cahen, D.; Hodes, G. How Important Is the Organic Part of Lead Halide Perovskite Photovoltaic Cells? Efficient CsPbBr3 Cells. *The Journal of Physical Chemistry Letters* **2015**, *6*, 2452–2456.

(40) Møller, C. K. Crystal Structure and Photoconductivity of Cesium Plumbohalides. *Nature* **1958**, *182*, 1436.

(41) Mattoni, A.; Filippetti, A.; Saba, M. I.; Delugas, P. Methylammonium Rotational Dynamics in Lead Halide Perovskite by Classical Molecular Dynamics: The Role of Temperature. *The Journal of Physical Chemistry C* **2015**, *119*, 17421–17428.

(42) Beck, H.; Gehrmann, C.; Egger, D. A. Structure and binding in halide perovskites: Analysis of static and dynamic effects from dispersion-corrected density functional theory. *APL Materials* **2019**, *7*, 021108.

(43) Leguy, A. M. A.; Frost, J. M.; McMahon, A. P.; Sakai, V. G.; Kockelmann, W.; Law, C.; Li, X.; Foglia, F.; Walsh, A.; O'Regan, B. C.; Nelson, J.; Cabral, J. T.; Barnes, P. R. F. The dynamics of methylammonium ions in hybrid organic–inorganic perovskite solar cells. *Nature Communications* **2015**, *6*.

(44) Weadock, N. J.; MacKeen, C.; Qin, X.; Waquier, L.; Rakita, Y.; Vigil, J. A.; Karunadasa, H. I.; Blum, V.; Toney, M. F.; Bridges, F. Thermal Contributions to the Local and Long-Range Structural Disorder in $CH_3NH_3PbBr_3$. *PRX Energy* **2023**, *2*, 033004.

(45) Wang, Y.; Liu, J.; Wang, J.; Fan, Z. Phase Stability and Transformations in CsSnI3: Is Anharmonicity Negligible? *The Journal of Physical Chemistry C* **2022**, *0*, null.

(46) da Silva, E. L.; Skelton, J. M.; Parker, S. C.; Walsh, A. Phase stability and transformations in the halide perovskite $CsSnI_3$. *Phys. Rev. B* **2015**, *91*, 144107.

(47) Dickel, D.; Daw, M. S. First-principles electronic structure in second-moment calculation of mode frequencies: Failure of quasiharmonic approximation in silicon. *Phys. Rev. B* **2019**, *100*, 214314.

(48) Brivio, F.; Frost, J. M.; Skelton, J. M.; Jackson, A. J.; Weber, O. J.; Weller, M. T.; Goñi, A. R.; Leguy, A. M. A.; Barnes, P. R. F.; Walsh, A. Lattice dynamics and vibrational spectra of the orthorhombic, tetragonal, and cubic phases of methylammonium lead iodide. *Phys. Rev. B* **2015**, *92*, 144308.

(49) Supasai, T.; Rujisamphan, N.; Ullrich, K.; Chemseddine, A.; Dittrich, T. Formation of a passivating CH3NH3PbI3/PbI2 interface during moderate heating of CH3NH3PbI3 layers. *Applied Physics Letters* **2013**, *103*, 183906.

(50) Heyd, J.; Scuseria, G. E.; Ernzerhof, M. Hybrid functionals based on a screened Coulomb potential. *J. Chem. Phys.* **2003**, *118*, 8207–8215.

(51) Heyd, J.; Scuseria, G. E.; Ernzerhof, M. Erratum "Hybrid functionals based on a screened Coulomb potential" [J. Chem. Phys. 118, 8207 (2003)]. *J. Chem. Phys.* **2006**, *124*, 219906.

(52) Tkatchenko, A.; Scheffler, M. Accurate Molecular Van Der Waals Interactions from Ground-State Electron Density and Free-Atom Reference Data. *Phys. Rev. Lett.* **2009**, *102*, 073005.

(53) Perdew, J. P.; Burke, K.; Ernzerhof, M. Generalized Gradient Approximation Made Simple. *Phys. Rev. Lett.* **1996**, *77*, 3865–3868.

(54) Adamo, C.; Barone, V. Toward reliable density functional methods without adjustable parameters: The PBE0 model. *Journal of Chemical Physics* **1999**, *110*, 6158 – 6170, Cited by: 11190.

(55) Liu, C.; Huhn, W.; Du, K.-Z.; Vazquez-Mayagoitia, A.; Dirkes, D.; You, W.; Kanai, Y.; Mitzi, D. B.; Blum, V. Tunable Semiconductors Control over Carrier States and Excitations in Layered Hybrid Organic-Inorganic Perovskites. *Phys. Rev. Lett.* **2018**, *121*, 146401.

(56) Jana, M. K.; Janke, S. M.; Dirkes, D. J.; Dovletgeldi, S.; Liu, C.; Qin, X.; Gundogdu, K.; You, W.; Blum, V.; Mitzi, D. B. Direct-Bandgap 2D Silver–Bismuth Iodide Double Perovskite: The Structure-Directing Influence of an Oligothiophene Spacer Cation. *Journal of the American Chemical Society* **2019**, *141*, 7955–7964, PMID: 31017429.

(57) Jana, M. K.; Liu, C.; Lidin, S.; Dirkes, D. J.; You, W.; Blum, V.; Mitzi, D. B. Resolving Rotational Stacking Disorder and Electronic Level Alignment in a 2D Oligothiophene-Based Lead Iodide Perovskite. *Chemistry of Materials* **2019**, *31*, 8523–8532.

(58) Wright, N. E.; Qin, X.; Xu, J.; Kelly, L. L.; Harvey, S. P.; Toney, M. F.; Blum, V.; Stiff-Roberts, A. D. Influence of Annealing and Composition on the Crystal Structure of Mixed-Halide, Ruddlesden–Popper Perovskites. *Chemistry of Materials* **2022**, *34*, 3109–3122.

(59) Song, R.; Liu, C.; Kanai, Y.; Mitzi, D. B.; Blum, V. Structure and electronic tunability of acene alkylamine based layered hybrid organic-inorganic perovskites from first principles. *Phys. Rev. Mater.* **2023**, *7*, 084601.

(60) Park, J. Y.; Song, R.; Liang, J.; Jin, L.; Wang, K.; Li, S.; Shi, E.; Gao, Y.; Zeller, M.; Teat, S. J.; Guo, P.; Huang, L.; Zhao, Y. S.; Blum, V.; Dou, L. Thickness control of organic semiconductor-incorporated perovskites. *Nature Chemistry* **2023**, https://doi.org/10.1038/s41557–023–01311–0.

(61) Ambrosetti, A.; Reilly, A. M.; DiStasio, R. A.; Tkatchenko, A. Long-range correlation energy calculated from coupled atomic response functions. *The Journal of Chemical Physics* **2014**, *140*, 18A508.

(62) Fedorov, D. V.; Sadhukhan, M.; Stöhr, M.; Tkatchenko, A. Quantum-Mechanical Relation between Atomic Dipole Polarizability and the van der Waals Radius. *Phys. Rev. Lett.* **2018**, *121*, 183401.

(63) Kim, Y.-H.; Song, R.; Hao, J.; Zhai, Y.; Yan, L.; Moot, T.; Palmstrom, A. F.; Brunecky, R.; You, W.; Berry, J. J.; Blackburn, J. L.; Beard, M. C.; Blum, V.; Luther, J. M. The Structural Origin of Chiroptical Properties in Perovskite Nanocrystals with Chiral Organic Ligands. *Advanced Functional Materials* **2022**, *32*, 2200454.

(64) Piccini, G.; Alessio, M.; Sauer, J.; Zhi, Y.; Liu, Y.; Kolvenbach, R.; Jentys, A.; Lercher, J. A. Accurate Adsorption Thermodynamics of Small Alkanes in Zeolites. Ab initio Theory and Experiment for H-Chabazite. *The Journal of Physical Chemistry C* **2015**, *119*, 6128–6137.

(65) Rybicki, M.; Sauer, J. Rigid Body Approximation for the Anharmonic Description of Molecule–Surface Vibrations. *Journal of Chemical Theory and Computation* **2022**, *18*, 5618–5635, PMID: 35913469.

(66) Capitani, F.; Marini, C.; Caramazza, S.; Postorino, P.; Garbarino, G.; Hanfland, M.; Pisanu, A.; Quadrelli, P.; Malavasi, L. High-pressure behavior of methylammonium lead iodide (MAPbI3) hybrid perovskite. *Journal of Applied Physics* **2016**, *119*, 185901.

(67) Weller, M. T.; Weber, O. J.; Henry, P. F.; Pumpo, A. M. D.; Hansen, T. C. Complete structure and cation orientation in the perovskite photovoltaic methylammonium lead iodide between 100 and 352 K. *Chem. Commun.* **2015**, *51*, 4180.

(68) Lahnsteiner, J.; Kresse, G.; Kumar, A.; Sarma, D. D.; Franchini, C.; Bokdam, M. Room-temperature dynamic correlation between methylammonium molecules in lead-iodine based perovskites: An ab initio molecular dynamics perspective. *Phys. Rev. B* **2016**, *94*, 214114.

(69) Lahnsteiner, J.; Kresse, G.; Heinen, J.; Bokdam, M. Finite-temperature structure of the $MAPbI_3$ perovskite: Comparing density functional approximations and force fields to experiment. *Phys. Rev. Mater.* **2018**, *2*, 073604.

(70) Havu, V.; Blum, V.; Havu, P.; Scheffler, M. Efficient O(N) integration for all-electron electronic structure calculation using numeric basis functions. *Journal of Computational Physics* **2009**, *228*, 8367–8379.

(71) Lejaeghere, K. et al. Reproducibility in density functional theory calculations of solids. *Science* **2016**, *351*, aad3000.

(72) Jensen, S. R.; Saha, S.; Flores-Livas, J. A.; Huhn, W.; Blum, V.; Goedecker, S.; Frediani, L. The Elephant in the Room of Density Functional Theory Calculations. *The Journal of Physical Chemistry Letters* **2017**, *8*, 1449–1457, PMID: 28291362.

(73) Knuth, F.; Carbogno, C.; Atalla, V.; Blum, V.; Scheffler, M. All-electron formalism for total energy strain derivatives and stress tensor components for numeric atom-centered orbitals. *Computer Physics Communications* **2015**, *190*, 33–50.

(74) Popolitov V.I., P. G. Synthesis of single-crystalline lead compounds under hydrothermal conditions. *Inorganic Materials (translated from Neorganicheskie Materialy)* **1991**, *27*, 2247–2251.

(75) Krukau, A. V.; Vydrov, O. A.; Izmaylov, A. F.; Scuseria, G. E. Influence of the exchange screening parameter on the performance of screened hybrid functionals. *The Journal of Chemical Physics* **2006**, *125*, 224106.

(76) Wyckoff, R. W. G. *Crystal Structures 1*, 2nd ed.; Crystal Structures; Interscience Publishers: New York, New York, 1963; Vol. 1.

(77) Chutia, S.; Rossi, M.; Blum, V. Water Adsorption at Two Unsolvated Peptides with a Protonated Lysine Residue: From Self-Solvation to Solvation. *The Journal of Physical Chemistry B* **2012**, *116*, 14788–14804, PMID: 23171405.

(78) Togo, A.; Tanaka, I. First principles phonon calculations in materials science. *Scr. Mater.* **2015**, *108*, 1–5.

(79) Aguiar-Ricardo, A.; Duarte, C.; Nunes da Ponte, M.; Marsh, K.; Stølen, S. In *Measurement of the Thermodynamic Properties of Single Phases*; Goodwin, A., Marsh, K., Wakeham, W., Eds.; Experimental Thermodynamics; Elsevier, 2003; Vol. 6; pp 387–432.

(80) Knudsen, M. Die Molekularströmung der Gase durch Offnungen und die Effusion. *Annalen der Physik* **1909**, *333*, 999–1016.

(81) Perdew, J. P.; Ernzerhof, M.; Burke, K. Rationale for mixing exact exchange with density functional approximations. *The Journal of Chemical Physics* **1996**, *105*, 9982–9985.

(82) Whitfield, P. S.; Herron, N.; Guise, W. E.; Page, K.; Cheng, Y. Q.; Milas, I.; Crawford, M. K. Structures, Phase Transitions and Tricritical Behavior of the Hybrid Perovskite Methyl Ammonium Lead Iodide. *Scientific Reports* **2016**, *6*.

(83) Jacobsson, T. J.; Schwan, L. J.; Ottosson, M.; Hagfeldt, A.; Edvinsson, T. Determination of Thermal Expansion Coefficients and Locating the Temperature-Induced Phase Transition in Methylammonium Lead Perovskites Using X-ray Diffraction. *Inorganic Chemistry* **2015**, *54*, 10678–10685, PMID: 26457861.

(84) Suryanarayana, S. V.; Deshpande, V. T. X-RAY DETERMINATION OF THE THERMAL EXPANSION OF LEAD MOLYBDATE. *Current Science* **1972**, *41*, 837–839.

(85) Sears, W. M.; Klein, M. L.; Morrison, J. A. Polytypism and the vibrational properties of PbI_2. *Phys. Rev. B* **1979**, *19*, 2305–2313.

(86) Lu, H. et al. Electronic Impurity Doping of a 2D Hybrid Lead Iodide Perovskite by Bi and Sn. *PRX Energy* **2023**, *2*, 023010.

(87) McQuarrie, D. *Quantum Chemistry*; University Science Books, 2008.